Cell

Skeletal Muscle Performance Determined by Modulation of Number of Myosin Motors Rather Than Motor Force or Stroke Size

Gabriella Piazzesi,[1,2] Massimo Reconditi,[1] Marco Linari,[1] Leonardo Lucii,[1] Pasquale Bianco,[1,2] Elisabetta Brunello,[1,2] Valérie Decostre,[1] Alex Stewart,[3] David B. Gore,[4] Thomas C. Irving,[4] Malcolm Irving,[5,*] and Vincenzo Lombardi[1,2]

[1]Laboratorio di Fisiologia, Dipartimento di Biologia Animale e Genetica, Università degli Studi di Firenze, Via G. Sansone 1, 50019 Sesto Fiorentino, Italy
[2]CRS SOFT-INFM-CNR, Università di Roma "La Sapienza", 00185 Roma, Italy
[3]Dexela Ltd., Spitfire Studios, 63 Collier Street, London N1 9BE, UK
[4]BioCAT, Advanced Photon Source, 9700 South Cass Avenue, Argonne, IL 60439 , USA
[5]Randall Division of Cell and Molecular Biophysics, King's College London, London SE1 1UL, UK
*Correspondence: malcolm.irving@kcl.ac.uk
DOI 10.1016/j.cell.2007.09.045

SUMMARY

Skeletal muscle can bear a high load at constant length, or shorten rapidly when the load is low. This force-velocity relationship is the primary determinant of muscle performance in vivo. Here we exploited the quasi-crystalline order of myosin II motors in muscle filaments to determine the molecular basis of this relationship by X-ray interference and mechanical measurements on intact single cells. We found that, during muscle shortening at a wide range of velocities, individual myosin motors maintain a force of about 6 pN while pulling an actin filament through a 6 nm stroke, then quickly detach when the motor reaches a critical conformation. Thus we show that the force-velocity relationship is primarily a result of a reduction in the number of motors attached to actin in each filament in proportion to the filament load. These results explain muscle performance and efficiency in terms of the molecular mechanism of the myosin motor.

INTRODUCTION

The myosin II motors that drive muscle contraction are organized into ordered superstructures in which a large ensemble of motors acts as a functional unit. The α-helical tails of the myosin II molecules are packed into the backbone of myosin filaments, with groups of motors emerging at regular 14.5 nm intervals (Huxley and Brown, 1967; Figure 1A). Relative sliding of actin and myosin filaments during muscle contraction is driven by the motor ensemble, mechanically coupled by their connections to the filament backbone and structurally constrained by the locally ordered lattice of parallel filaments (Hanson and Huxley, 1953; Huxley, 1969). This structure is repeated regularly along the muscle cell, with an array of myosin filaments at the midpoint of each muscle sarcomere. Each myosin molecule contains two identical motors composed of a catalytic domain that attaches to actin in a well-defined orientation and a light-chain domain that connects the catalytic domain to the myosin tail and filament (Figure 1B; Rayment et al., 1993a). Crystallographic studies suggest that the working stroke of the motor is produced by bending between these two domains, so that tilting of the light-chain domain drives relative sliding between the myosin and actin filaments (Rayment et al., 1993b; Holmes, 1997; Dominguez et al., 1998).

The quasi-crystalline structure and organization of the myosin filaments allow the motor mechanism to be characterized with remarkably high structural and temporal resolution in an intact muscle cell by a combination of mechanical and X-ray techniques (Huxley and Simmons, 1971; Piazzesi et al., 2002a, 2002b; Reconditi et al., 2004). Previously, these techniques relied on fast perturbations of muscle cell length or force to synchronize the action of the motor ensemble. The physiological performance of muscle, however, depends on asynchronous action of the motors on a slower timescale. Here we applied the combined mechanical and X-ray approach to determine the molecular basis of the primary determinant of muscle performance in vivo: the relationship between shortening velocity and load. The results do not support the conventional explanation of this relationship (Huxley, 1957; Cooke, 1997), in which the lower force exerted by shortening muscle is primarily a result of a lower force per motor. We propose a quantitative explanation of muscle performance and efficiency in terms of the unitary action of an individual myosin motor which integrates previous mechanistic insights from mechanical and structural studies at both the cellular and molecular levels.
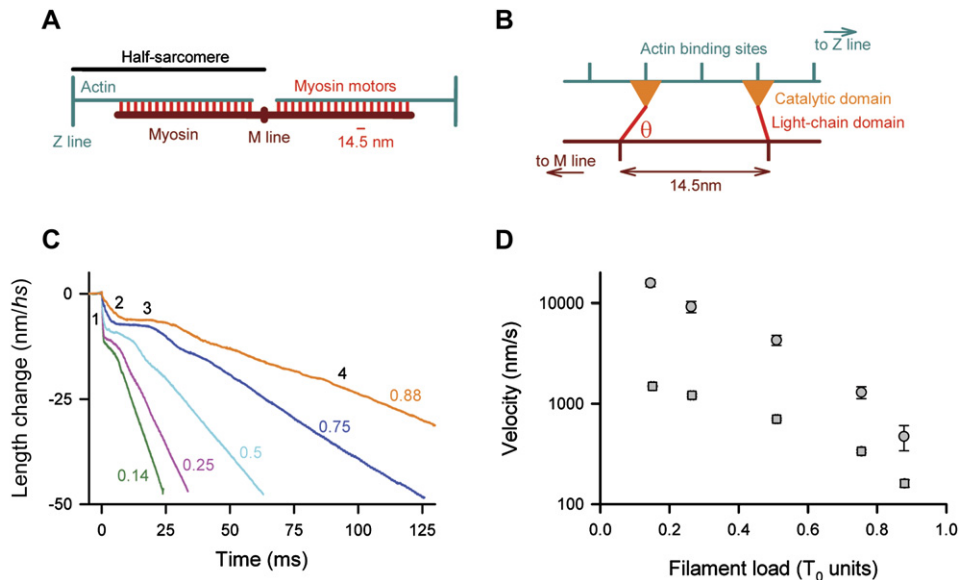
Figure 1. Structure and Function of Myosin Motors in Skeletal Muscle
(A) Organization of myosin and actin filaments in the muscle sarcomere.
(B) Conformation of myosin motors attached to actin.
(C) Four kinetic phases of half-sarcomere (*hs*) shortening following steps to the loads indicated.
(D) Filament sliding velocity during shortening against different filament loads in phase 2 (circles) and phase 4 (squares).
Error bars denote SE of mean.

RESULTS

The Motor Action of Muscle Myosin II Is Faster at Low Filament Load

The molecular basis of the force-velocity relationship in skeletal muscle is most clearly revealed by suddenly decreasing the load on an active single muscle cell to a fraction of its isometric value (Figure 1C). The load step triggers a velocity transient with four phases (black numbers on the upper trace). During the load step itself, which is complete in about 120 μs, the muscle fiber shortens elastically (phase 1). It continues to shorten rapidly for a few milliseconds after the load step is complete (phase 2). Shortening then slows or even stops (phase 3) before accelerating to the steady velocity (phase 4) characteristic of each load, indicated in color by the side of each trace in Figure 1C.

Filament sliding is much faster in phase 2 (Figure 1D, circles) than in phase 4 (squares), but in both phases sliding is faster at lower load. The phase 4 velocity-load relationship represents a steady state in which motors are repeatedly attaching to actin, stroking and then detaching from actin; this relationship determines muscle performance on the physiological timescale. Phase 2, in contrast, is produced by a synchronous working stroke in myosin motors that were attached to actin before the load step (Piazzesi et al., 2002a; Reconditi et al., 2004). Phase 2 is not directly relevant to muscle function in vivo, but analysis of the phase 2 and 4 responses together reveals the underlying molecular basis of muscle performance, as

shown below. Phases 2 and 4 have not been reliably separated previously in either whole-muscle or single-molecule experiments, although they are clearly resolved at the single-cell level.

Myosin Motors Move toward the Sarcomeric M Line during Muscle Shortening

The regular arrangement of myosin molecules at 14.5 nm intervals along the myosin filaments in the muscle sarcomere (Figure 1A) produces an X-ray reflection called the M3. Because this X-ray reflection is sensitive to the periodic mass distribution of the motors along the filaments, it can be used to measure nanometer-scale changes in the conformation of actin-attached motors during the working stroke (Huxley et al., 1983; Irving et al., 2000a). The intensity of the M3 reflection (I_{M3}) decreases during phase 2 of the response to a load step (Figure 2A, circles), as myosin motors tilt during the working stroke (Reconditi et al., 2004). There is little recovery of I_{M3} during phase 3 (triangles), and it remains constant during steady phase 4 shortening (squares). The average value of I_{M3} during steady shortening against different loads is approximately proportional to the load (Figure 2B).

The lower intensity of the M3 reflection during faster phase 4 shortening against a lower load indicates that the motor mass is more spread out along the filaments. This might be a result of either tilting of their light-chain domains (Figure 1B) or an increase in the axial dispersion of the motor population. The relative contribution of these two factors was determined by X-ray interference. Because each
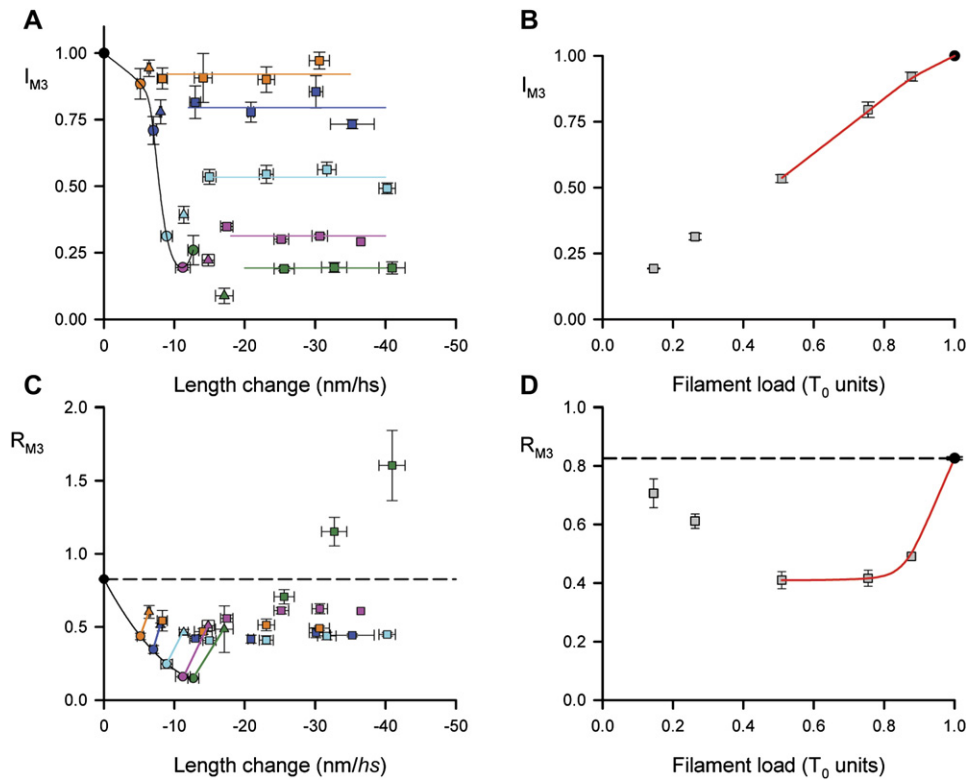
Figure 2. Changes in the M3 X-Ray Reflection following a Load Step

(A and B) Intensity of the M3 reflection, plotted in (A) against half-sarcomere shortening and in (B) against load. Circles, triangles, and squares denote phases 2, 3, and 4 of the velocity transient, respectively.

(C and D) Ratio of the two interference peaks of the M3 reflection plotted against half-sarcomere shortening and load, respectively; values in (D) were recorded early in phase 4.

Colors in (A) and (C) denote the loads in Figure 1C. Error bars denote standard error (SE) of mean.

myosin filament contains two regular arrays of motors, one on either side of the filament midpoint or M line (Figure 1A), X-rays scattered by the two arrays interfere, splitting the M3 reflection into two component peaks. The ratio R_{M3} of the intensities of these two peaks measures the average axial motion of motors toward the M line with subnanometer resolution, but is relatively independent of their axial dispersion (Linari et al., 2000; Piazzesi et al., 2002b; Reconditi, 2006; Reconditi et al., 2004; Huxley et al., 2006a).

R_{M3} decreases during phases 1 and 2 of the response to a load step (Figure 2C, circles), signaling axial motion of motors toward the M line during the working stroke (Reconditi et al., 2004). It then partially recovers during phase 3 (triangles), as motors detach from the original actin binding sites and attach to new sites further from the M line. During phase 4 shortening at medium or high load, R_{M3} remains below its isometric value (Figure 2C, squares; Figure 2D; Huxley et al., 2006b), showing that the motors are displaced toward the M line, consistent with an increase in the average angle (θ) between the light-chain domain and the filament axis (Figure 1B). R_{M3} has a strongly nonlinear dependence on the load (Figure 2D), suggesting that the faster phase 4 shortening at lower load is not accompanied by a proportional increase in the motor stroke.

At the lowest load studied (0.14 times the isometric value T_0; Figure 2C, green squares), there was a large progressive increase in R_{M3} during steady shortening, indicating motion of motors *away* from the M line. At the same time the spacing of the M3 reflection (S_{M3}) decreased significantly, indicating a progressive change in myosin filament structure (Piazzesi et al., 1999; see also Supplemental Data available with this article online). At higher loads S_{M3} was constant during steady shortening, and its load dependence was equal to that expected from the 0.26%/T_0 compliance of the myosin filament (Reconditi et al., 2004). The anomalous behavior of R_{M3} and S_{M3} at the lowest load shows that, despite the constant shortening velocity observed under these conditions, the structure of the myosin filament progressively reverts toward that observed in resting muscle. This phenomenon was not observed during shortening at loads of 0.25 times the isometric value or higher.

The Elastic Strain of Single Myosin Motors during Muscle Shortening

In order to determine the size of the motor stroke from the structural data described above, we need to know the number of motors attached to actin at each load. We
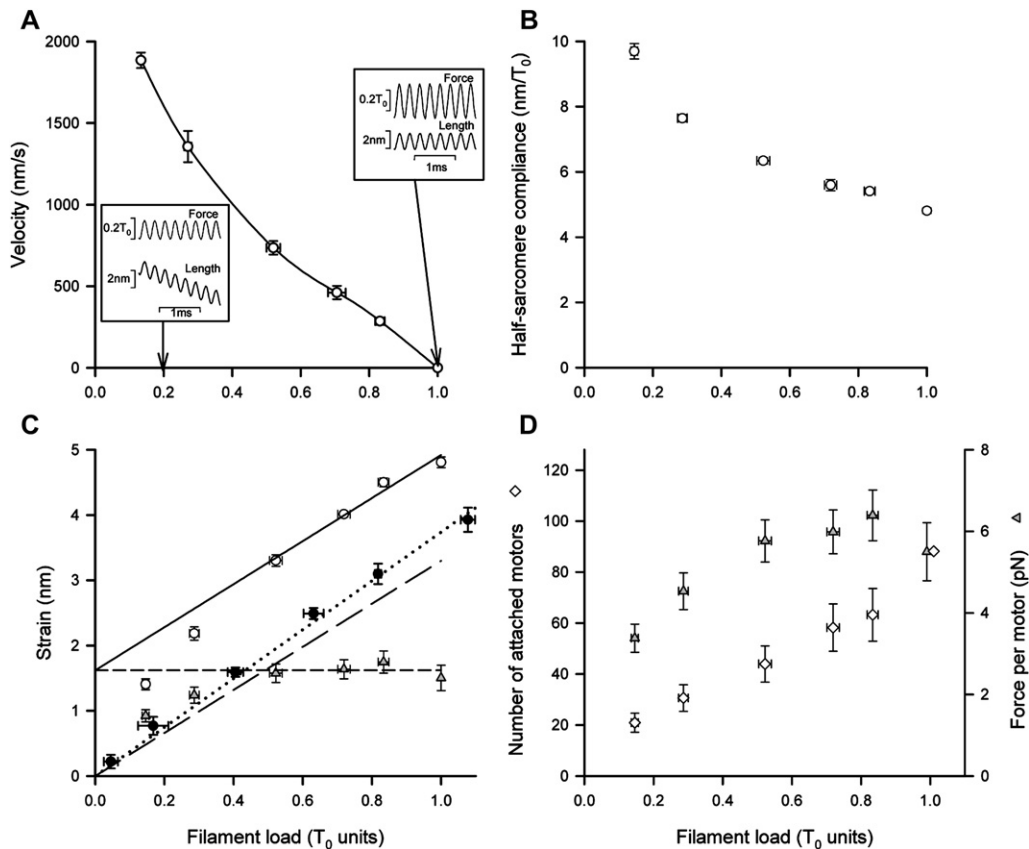
Figure 3. Myosin Motor Mechanics during Steady Shortening against Different Loads

(A) Steady shortening velocity. Insets: changes in fiber force and half-sarcomere length during 4 kHz oscillations superimposed on isometric contraction (right) and steady shortening at 0.2 T_0 (left). Velocity at zero load was estimated as 2750 ± 90 nm/s from a hyperbolic fit of the data for loads < 0.8 T_0.

(B) Compliance of the half-sarcomere.

(C) Half-sarcomere strain (circles) and motor strain (triangles); open symbols and continuous line denote active contraction; filled circles and dotted line denote rigor; the long dashed line is the filament compliance.

(D) Number of myosin motors in each myosin half-filament attached to actin (diamonds) and force per actin-attached motor (triangles).

Error bars denote SE of mean.

measured this number by imposing small length oscillations on an active single muscle cell (Figure 3A, insets) at 4 kHz, much faster than the motor stroke. The compliance of each set of myosin and actin filaments and the motors that crosslink them (the half-sarcomere, *hs*; Figure 1A) is the ratio of the synchronous 4 kHz length and force changes observed in this experiment. At the isometric force (T_0; right inset), this ratio is smaller than during steady phase 4 shortening against low load (left inset). The *hs* compliance was 4.9 nm/T_0 during isometric contraction (Figure 3B; Ford et al., 1977) and roughly twice this value during fast shortening against a load of 0.15 T_0, indicating that fewer motors are attached to actin during shortening. The number of attached motors can be calculated from the *hs* strain (i.e., compliance times load) at each load (Figure 3C, open circles). During steady shortening at loads greater than 0.5 T_0, the *hs* strain decreased linearly with decreasing load (continuous black line), with a slope of 3.2 nm/T_0, corresponding to 0.013 nm/kPa in the group

of fibers used in these experiments. This slope is a compliance, and is equal to the compliance of the myosin and actin filaments measured by X-ray diffraction (Huxley et al., 1994; Wakabayashi et al., 1994; Dobbie et al., 1998; Reconditi et al., 2004). The elastic strain in the myosin motors was calculated by subtracting the contribution of filament strain (long dashed line) from the *hs* strain (open circles). The motor strain (triangles) was roughly constant at around 1.7 nm at medium to high load, but was reduced at low load.

The Compliance of a Single Motor

The compliance of a single motor (c_m) is equal to its strain divided by the motor force. We determined c_m from the *hs* compliance of muscle fibers that had been depleted of ATP to produce a "rigor" state in which all 294 motors in each half-filament are attached to actin (Craig, 1977; Cooke and Franks, 1980; Linari et al., 1998). The *hs* strain in rigor was directly proportional to
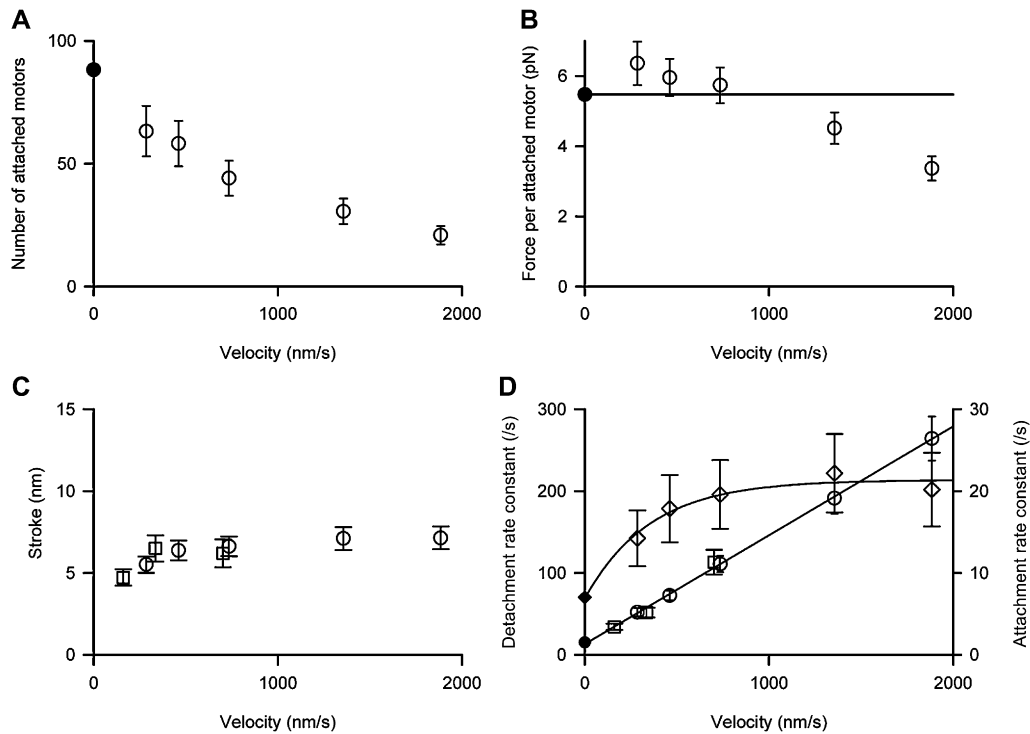
Figure 4. Molecular Basis of the Relationship between Force and Velocity during Steady Shortening
(A) Number of motors attached to actin in each myosin half-filament.
(B) Force per attached motor.
(C) Sliding distance L over which a motor remains attached, estimated from X-ray (squares) and mechanical (circles) data.
(D) Apparent attachment rate constants (diamonds) and detachment rate constants (squares, from X-ray data; circles, from mechanics).
Error bars denote SE of mean.

the load (Figure 3C, filled circles), as expected for a linear elasticity. The slope of this relationship, corresponding to the compliance of a half-sarcomere with all motors attached, was 3.7 ± 0.1 nm/T_0. The filaments contribute 3.2 nm/T_0 as discussed above, so the motor strain when all motors are attached to actin is 0.5 nm/T_0. The isometric force (T_0), calculated from the macroscopic stress and filament lattice dimensions, is 480 pN in each myosin half-filament (Lombardi et al., 1992). Because the 294 motors in the half-filament are mechanically in parallel, each motor bears a force of 480/294 or 1.6 pN under these conditions, and the compliance of an individual myosin motor (c_m) is 0.5/1.6, or 0.3 nm/pN. The same value of c_m for myosin motors in intact muscle fibers was recently determined by an independent method that did not involve induction of the rigor state (Decostre et al., 2005), suggesting that $c_m = 0.3$ nm/pN is a fundamental elastic constant of the myosin motor that is independent of the presence of ATP. This value is lower than that measured in mechanical studies on single myosin molecules (Veigel et al., 1998; Smith et al., 2001; Takagi et al., 2006; Capitanio et al., 2006), probably because of the additional compliance of the connections between the myosin and the transducers in the in vitro studies.

Individual Motors Exert a Force of 6 pN during Slow- and Medium-Velocity Shortening

The motor strain during isometric contraction is 1.7 nm (Figure 3C, triangle at T_0), so the unitary force per motor under these conditions can be calculated as the motor strain divided by c_m, that is, 1.7/0.3, or 5.7 pN. The force borne by each half-filament is 480 pN, as noted above, so the number of motors attached to actin (N) during isometric contraction is 480/5.7 = 84 (Figure 3D, diamond at T_0), about 30% of the total number of motors present in each half-filament.

The force per motor during steady shortening was calculated from the corresponding motor strain (Figure 3C, triangles). In the high-load region the force per motor is approximately constant, with a value of about 6 pN, and only falls below 4 pN at very low load, corresponding to very fast shortening (Figure 3D, triangles). The number of motors bound to actin (N) during shortening decreases almost linearly with decreasing load (Figure 3D, diamonds). Thus, the motor ensemble responds to a decrease in the external load with a decrease in the number of motors bound to actin rather than a decrease in the force per motor. The number of attached motors and the force per motor are plotted against the filament sliding velocity in Figures 4A and 4B, respectively.

Motors Execute a Six Nanometer Stroke during Slow- and Medium-Velocity Shortening

We calculated the motion of the attached motors from the X-ray data (Figure 2) and the number attached (Figure 3D) using a structural model of the working stroke (Rayment et al., 1993a, 1993b; Holmes, 1997; Dominguez et al., 1998) in which the light-chain domain of the motor tilts with respect to the actin-attached catalytic domain (Figure 1B). We calculated the axial mass distribution of the motors for a distribution of orientations (θ) of the light-chain domain with mean $<\theta>$ and uniform dispersion $\pm \delta$. During isometric contraction the actin-attached 30% of motors have $<\theta> = 60°$, $\delta = 17°$ (Reconditi et al., 2004), and the detached 70% were represented by a Gaussian axial mass distribution with the center (x_g) 1.2 nm closer to the M line than the center of mass of the attached heads, and standard deviation $\sigma = 3.6$ nm. These parameters were chosen to reproduce the changes in R_{M3} and I_{M3} in phases 1 and 2 of the response to a length or load step (Irving et al., 2000a; Piazzesi et al., 2002b; Reconditi et al., 2004), during which the number of attached motors is almost constant. Because the axial displacement of the motors during phases 1 and 2 can be calculated from the size of the length or load step and the filament compliances, those data provide an in situ calibration of the X-ray interference method. The X-ray data for steady shortening can then be interpreted directly in terms of the change in the mean orientation of the light-chain domain $<\theta>$ with no remaining free parameters. The additional detached motors during steady shortening were assumed to have the same mass distribution as the detached motors during isometric contraction.

The experimental values of R_{M3} and I_{M3} during steady phase 4 shortening at loads of 0.88 T_0 and 0.75 T_0 were fitted by $<\theta> = 75°$ and 81°, respectively, with the dispersion δ remaining at its isometric value, 17° (Figures 2B and 2D, red line). Thus, these high-load data suggest that the non-linearity of the R_{M3} versus load relationship is because of an underlying nonlinearity in the relationship between $<\theta>$ and load. R_{M3} and I_{M3} for 0.5 T_0 were fitted by $<\theta> = 80°$, $\delta = 17°$, with the dispersion of the detached motors (σ) increased slightly to 3.88 nm. At loads lower than 0.5 T_0 it was not possible to determine a unique value of $<\theta>$ because of the low fraction of motors attached. The progressive increase in R_{M3} during steady shortening at 0.14 T_0 (Figure 2C, green squares) could only be reproduced by a change in x_g, indicating motion of the detached motors away from the M line. This process is associated with a change in the myosin filament periodicity as discussed above, and is not present at higher loads.

The fitted values of $<\theta>$ during steady shortening at loads of 0.88, 0.75, and 0.5 T_0 correspond to mean displacements $<x>$ of the catalytic domain from its isometric position toward the M line by 2.4, 3.3, and 3.1 nm, respectively. Assuming that, during shortening, motors attach in the isometric conformation and remain attached over a filament sliding distance L, their mean displacement from the isometric position $<x>$ is $L/2$. Based on the values of $<x>$ estimated above, L is 5–7 nm during shortening at loads between 0.5 and 0.88 T_0. In this range, L has little dependence on load or on filament sliding velocity (Figure 4C, squares).

The Six Nanometer Motor Stroke Is Consistent with Muscle Energetics

We obtained an independent estimate of L from the mechanical results (Figure 3), under the assumption that one ATP molecule is hydrolyzed for each cycle of motor attachment to actin. The free energy of ATP hydrolysis is 85 zJ, and the efficiency of its conversion to mechanical work is 0.45 at high load, decreasing to 0.38 and 0.28 at 0.25 and 0.14 T_0, respectively (Dawson et al., 1978; Linari and Woledge, 1995; Barclay, 1998). Thus, the work per cycle of motor attachment (W) is 38 zJ at high load, decreasing to 24 zJ at 0.14 T_0. L is then calculated as W divided by the force per motor (Figure 4B), giving values in the range of 5–7 nm (Figure 4C, circles). These estimates of L from mechanics are in good agreement with those from the X-ray data (squares).

Kinetics of the Motor Cycle during Steady Shortening

Rapid detachment of motors from actin at the end of the working stroke was implicit in the above estimates of L, and it follows that the effective detachment rate constant (g_{APP}; Figure 4D, circles and squares) can be estimated as V/L, where V is the filament sliding velocity. g_{APP} increases almost linearly with shortening velocity, as expected from the relative constancy of L. The effective attachment rate constant (f_{APP}; diamonds) in a simple two-state cycle was then calculated from g_{APP} and the fraction of motors attached (Figure 4A). The corresponding rate constants for isometric contraction (Figure 4D, filled symbols) were estimated from the fraction attached and the isometric rate of ATP utilization (5/s; Linari and Woledge, 1995). These isometric rate constants lie on the extrapolations of the rate constant-velocity relationships for steady shortening (Figure 4D).

The rate of ATP utilization, calculated for any velocity as $f_{APP} * g_{APP}/(f_{APP} + g_{APP})$, increases to about 11/s during shortening at 300 nm/s and 19/s at 1900 nm/s. Although the increase in the rate of ATP utilization with shortening velocity is relatively modest, the extent of filament sliding during one ATP hydrolysis cycle increases from 26 to 100 nm in the same velocity range. The latter value illustrates the functional advantage of the ensemble organization of myosin motors to minimize the metabolic cost of low-load shortening by reducing the number of motors bound to actin.

DISCUSSION

A Molecular Explanation for the Force-Velocity Relationship of Skeletal Muscle

Conventional explanations of the force-velocity relationship (Huxley, 1957; Cooke, 1997) are founded on the

Cell

concept that sliding between the myosin and actin filaments in the direction corresponding to muscle shortening reduces the elastic force in the myosin motors that cross-link the filaments as external work is performed. The present results, in contrast, show that each motor maintains a force of about 6 pN, equal to the isometric force, during shortening at low to medium velocities (Figure 4B). Moreover, individual motors have a low compliance, and their elastic strain under the isometric force of 5.7 pN is only 1.7 nm (Figure 3), corresponding to an elastic energy of 0.5 * 1.7 * 5.7, or about 5 zJ. This is much smaller than the 38 zJ work output of a myosin motor in a single cycle of attachment, so the work done by shortening muscle cannot be explained by the discharge of elastic energy stored in the motor. The increase in the effective motor attachment rate (f_{APP}) with shortening velocity (Figure 4D) is also inconsistent with the original model (Huxley, 1957) and requires a more complex kinetic scheme, for example one in which the sequence of motor states in the ATPase cycle depends on the sliding velocity (Piazzesi and Lombardi, 1995). Saturation of f_{APP} indicates a rate-limiting transition at about 20/s between two detached states of the motor cycle.

We propose an alternative explanation for the force-velocity relationship which integrates the original concept of the motor attachment-detachment cycle (Huxley, 1957) with the subsequent proposal that active force is generated within the attached motor (Huxley and Simmons, 1971). During slow- and medium-velocity shortening, the tendency of filament sliding to reduce the motor force is counteracted by active force generation, so that each attached motor maintains the force that it is able to develop under isometric conditions. The number of attached motors decreases approximately in proportion to the external load (Figure 3D), and this can be explained by rapid detachment of motors at the end of their working stroke (Figure 4D; see also Lan and Sun, 2005). Because the stroke size is only weakly dependent on velocity, the effective detachment rate increases almost linearly with velocity, so the number attached decreases. This mechanism explains the high efficiency of skeletal muscle over a wide range of physiological shortening velocities in a straightforward way: individual attached motors perform the same 6 pN × 6 nm stroke throughout this range, and the *number* of attached motors is modulated to match the external load. The sliding velocity at which this match occurs is set by the attachment rate.

The Force-Velocity Relationship of a Single Myosin Motor

The force per motor is smaller during faster phase 4 shortening (Figure 5A, squares). Essentially the same relationship between force per motor and filament sliding velocity is observed during phase 2 of the velocity transient following a load step (Figure 5A, circles; Piazzesi et al., 2002a). The two responses reveal the same underlying relationship between force and stroke rate in an individual motor molecule, extended to lower forces by the phase 2 data.
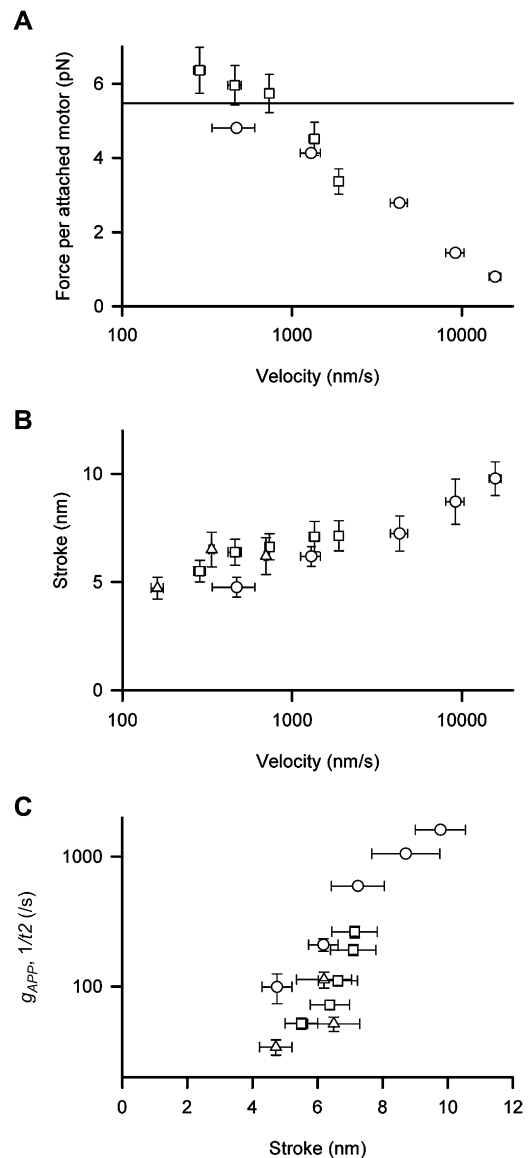
Figure 5. Molecular Parameters of the Myosin II Motor Mechanism

(A) Force-velocity relationship of a single motor.
(B) Dependence of motor stroke size on filament sliding velocity.
(C) Estimates of detachment rate constant as a function of motor stroke size. Circles, duration of phase 2 (1/t2); squares, g_{APP} from phase 4 mechanics; triangles, g_{APP} from phase 4 X-ray data.
Error bars denote SE of mean.

The motor is capable of driving filament sliding at 20,000 nm/s for about 0.5 ms when the motor force is suddenly reduced to 15% of its isometric value (circles in Figures 1D and 5A). The small difference between the phase 2 and phase 4 data in the high-force region is likely to be a result of an underestimation of motor force in phase 2 caused by fast detachment of a small fraction of motors (Lombardi et al., 1992; Piazzesi et al., 2002b).

The decrease in motor force at filament sliding velocities greater than about 1000 nm/s (Figure 5A) reflects the finite speed of the working stroke responsible for force generation in the actin-attached motor (Huxley and Simmons, 1971; Piazzesi et al., 2002a). The force per motor falls to about half its isometric value at a filament sliding velocity of ca 3000 nm/s, which is the velocity during phase 4 shortening against zero load. The intrinsic speed of the motor stroke is therefore well matched to its physiological function.

The Size of the Motor Stroke In Situ

A comparison of the stroke *amplitudes* in phases 2 and 4 provides further support for this molecular explanation of the force-velocity relationship. The phase 2 stroke is measured as the initial transient shortening of the half-sarcomere in the first few milliseconds after a sudden force decrease that synchronizes the motor strokes (Figure 1C; Piazzesi et al., 2002a), and is about 6 nm at high motor force (low velocity) and about 10 nm at low motor force (high velocity) (Figure 5B, circles), in agreement with previous structural estimates based on R_{M3} (Reconditi et al., 2004). The motor stroke during steady phase 4 shortening, defined as the extent of filament sliding over which the motor remains attached to actin, and calculated from either mechanical data (Figure 5B, squares) or R_{M3} and I_{M3} (Figure 5B, triangles), ranges from 5 to 7 nm. All these estimates of stroke size are in reasonable agreement, over the whole range of filament sliding velocity in either phase 2 or phase 4, and therefore over the whole range of force per motor (Figure 5A). The stroke size of the myosin II motor increases gradually by a factor of about two, from ca 5 to 10 nm, as the filament sliding velocity increases by two orders of magnitude, from ca 200 nm/s to 20,000 nm/s (Figure 5B).

Slightly larger estimates of stroke size in the low-velocity region, 7.5 nm at ca 100 nm/s and 10.0 nm at ca 1000 nm/s, were recently determined from measurements of R_{M3} and I_{M3} during steady shortening in whole muscles (Huxley et al., 2006b). Phases 2 and 4 cannot be resolved in that preparation, and there were several other differences in experimental protocols, temperature, and analysis between the whole-muscle and our single-cell studies. In particular, Huxley et al. estimated stroke size primarily from the axial dispersion of the attached motors, whereas we estimated it from the mean axial displacement. The small differences in the stroke size estimates from the two studies are likely to be due to these methodological differences.

This dependence of the stroke size of skeletal muscle myosin on sliding velocity (Figure 5B) and consequently on motor force (Figure 5A) is a fundamental characteristic of the myosin II motor mechanism. It is also a generic property of models in which the stroke is a result of a transition from one actin-attached state to another with lower free energy that is coupled to increased strain of an elastic element (Huxley and Simmons, 1971). In this paradigm, the effective stroke is reduced at high motor force because the energy required to stretch the elastic element reduces the equilibrium constant of the transition (Piazzesi et al., 2002a; Decostre et al., 2005). Quantitative analysis of this mechanism suggests that there must be more than two actin-attached states (Huxley and Simmons, 1971; Huxley and Tideswell, 1996), and the present results provide strong support for this requirement. Because the compliance of a single motor is 0.3 nm/pN, the energy required to extend the motor compliance in a single 10 nm stroke is 170 zJ, which is double the free energy available from ATP hydrolysis. This consideration makes any motor mechanism based on a single 10 nm stroke extremely unlikely, and shows that the 10 nm stroke observed at low load must be composed of a series of substrokes. The ca 6 nm stroke at high load can then be understood as a consequence of detachment from actin from an intermediate state in the series. A similar conclusion was derived previously from a theoretical analysis of the phase 4 force-velocity relationship in terms of the Huxley-Simmons formalism (Piazzesi and Lombardi, 1995).

The Rate of Motor Detachment from Actin Is Controlled by Motor Conformation

The weak dependence of motor stroke size on filament sliding velocity as the latter is varied over two orders of magnitude (Figure 5B) implies that the effective rate constant for detachment of the motor from actin is primarily determined by the extent of progress of the motor through its stroke. The effective detachment rate constant (g_{APP}) during steady phase 4 shortening is velocity divided by stroke size (Figure 4D). g_{APP} determined from either mechanical (Figure 5C, squares) or X-ray data (triangles) has a very steep dependence on stroke size. The corresponding detachment rate during phase 2 shortening cannot be determined by this approach because phase 2 is not a steady state, but an upper limit can be estimated as the reciprocal of the phase 2 duration (Figure 5C; $1/t2$, circles), which shows a steep dependence on stroke size similar to that of g_{APP}. Again, the phase 2 and 4 data point to the same underlying molecular mechanism, in which detachment of the motor from actin depends strongly on its progress through the stroke, and therefore on the conformation of the motor. The motor detaches from actin more quickly during faster shortening against a low filament load because it reaches the critical conformation for detachment more quickly.

The general concept that the motor detaches from actin only after performing useful work is closely related to its high efficiency (Huxley, 1957; Nyitrai and Geeves, 2004). In principle, the detachment rate might be controlled directly by the motor conformation (e.g., Lan and Sun, 2005), or by its load or elastic strain (e.g., Veigel et al., 2003; Takagi et al., 2006), and these two parameters are coupled in some theoretical formalisms. The present results show that the detachment rate varies by almost an order of magnitude during phase 4 shortening at slow to medium velocity while the force per motor is roughly constant (Figures 4B and 4D), which is inconsistent with

models in which the detachment rate is directly controlled by motor load or elastic strain. The results described above (Figure 5C) demonstrate that the detachment rate is specifically and directly controlled by motor conformation.

Relationship of the In Situ Stroke Size to Crystallographic Structures

X-ray crystallographic and electron microscopy studies of myosin fragments and their actin-bound complexes have revealed structural details of the motor mechanism in relation to its ATP hydrolysis cycle (Lymn and Taylor, 1971; Rayment et al., 1993a, 1993b; Dominguez et al., 1998; Holmes et al., 2003; Geeves and Holmes, 2005). The major structural change in the motor is a bend between its catalytic and light-chain domains, and this is associated with the release of the ATP hydrolysis products ADP and phosphate (Pi) from the active site of myosin, between the so-called *pre-power stroke* and *rigor-like* states. Although the structure of the actin-bound myosin-ADP-Pi complex has not been determined, it seems likely that in this state the catalytic domain would bind to actin as in the rigor-like state and, if so, tilting of the light-chain domain on release of the hydrolysis products would displace its distal end along the filament axis by 10–12 nm. This would produce a stroke size similar to that observed in situ when the motor load is suddenly reduced to very low values (Huxley and Simmons, 1971; Piazzesi et al., 2002a; Reconditi et al., 2004) and described above (Figure 5B). No intermediate states that might correspond to substrokes of the actin-attached motor have been identified by crystallographic studies of motor fragments in the absence of actin. However, these substates are likely to be both dynamic and significantly populated only under strain, in which case they would be effectively undetectable by current in vitro structural techniques.

Relation to In Vitro Mechanical Studies of the Myosin Motor

In vitro functional studies of single motor proteins have been particularly successful for motors like kinesin and myosin V that work as isolated molecules in the cellular environment. Muscle myosin II, in contrast, is designed to work within a quasi-crystalline ensemble, making it more difficult to compare the results of single-molecule and cell-level studies of myosin II. Moreover, the stroke rate of this myosin is ca 1000/s, which is too fast to be resolved or controlled by current single-molecule techniques, although these methods have demonstrated a load-dependent detachment rate for the much slower myosin II from smooth muscle (Veigel et al., 2003).

In the present work, we derived the molecular properties of skeletal muscle myosin II from high-resolution structural and functional studies of single muscle cells, under the working hypothesis that there are no unknown protein factors or phenomena contributing to the cellular responses. Where direct comparisons can be made, the in situ results are consistent with the in vitro properties of isolated muscle myosin II, supporting the working hypothesis. Thus, for example, mechanical studies on single molecules of muscle myosin II and its fragments have generally been interpreted in terms of a single working stroke of 5–6 nm at low motor load (Molloy et al., 1995; Tyska et al., 1999; Ruff et al., 2001; Steffen et al., 2001), and a recent analysis (Sleep et al., 2006) suggests that those studies may have underestimated the stroke size by a factor of two, which would make the in vitro mechanical estimates of the low-load stroke size 10–12 nm, in agreement with both the in vitro structural studies described above and the in situ values measured in the present work. Neither the high-load stroke nor the isometric force have been measured for single molecules of myosin II from skeletal muscle, but the average force at the end of single interactions under dynamic force feedback with a 1 ms time constant was ca 5 pN (Takagi et al., 2006), similar to the isometric force measured here. The *rate* of the myosin II stroke has not been measured in vitro.

The detachment rate of myosin II from actin in vitro is very much slower than the corresponding rate in situ at low load, about 1500/s (Figures 5A and 5C), because the ATP concentrations used in vitro are orders of magnitude smaller than the physiological value, so that motor detachment becomes limited by the rate of ATP binding. However, a recent in vitro study of fast myosin II from mouse muscle at 22°C (Capitanio et al., 2006) identified two components of the working stroke, the first of which was associated with a rate constant of 1200/s that was independent of ATP concentration, and might limit the rate of motor detachment at physiological [ATP]. This rate constant is close to that observed at low motor load in situ, and may reflect the same biochemical transition in the myosin II motor, most likely associated with ADP release from its active site.

The present results show that the fundamental determinant of muscle performance at the cellular level, the force-velocity relationship, can be understood at the level of the individual myosin II molecule. The organization of myosin II motors into ordered cellular ensembles allows physiological modulation of the number of motors attached to actin as a function of the filament load, which in turn allows individual motors to work at high force and efficiency against a wide range of external loads. Several fundamental properties of the myosin II motor reported here, including its isometric force, compliance, stroke dynamics, and detachment kinetics, can at present be measured only in situ. The general features of the myosin II motor mechanism described above, including the existence of substrokes and the control of detachment rate by motor conformation, are likely to be shared by other motor proteins.

EXPERIMENTAL PROCEDURES

Muscle Fibers and Mechanical Measurements

Single intact fibers were dissected from tibialis anterior muscles of frogs (*Rana temporaria*) that had been cooled to 2°C–4°C and killed by decapitation followed by destruction of the spinal cord. Fibers were mounted in Ringer's solution at 4°C and sarcomere length 2.1 μm between a capacitance force transducer and a loudspeaker-coil motor

(Lombardi and Piazzesi, 1990). Sarcomere length in a 1–1.5 mm fiber segment was measured continuously with a striation follower (Huxley et al., 1981). Fibers were stimulated every 4 min at 18–25 Hz via electrodes parallel to the fiber axis, for 0.4–2.3 s depending on the protocol. Force developed at constant fiber length and was clamped at the plateau level 240 ms after the first stimulus. Force steps were imposed 20 ms later. Force feedback parameters were optimized for each fiber and force-step amplitude. Force steps were complete in about 120 μs. The duration of phase 2 of the velocity transient following a force step (t2) was measured from the start of the step to the minimum value of the X-ray intensity ratio R_{M3} (see Figure 2b of Reconditi et al., 2004). The extent of filament sliding in this period is L2 but part of this, $s_{fil}.\Delta T$, is a result of the elasticity of the myosin and actin filaments, where s_{fil} is the filament strain during isometric contraction (3.2 nm; Figure 3) and ΔT is the decrease in force during the load step as a fraction of the isometric force. The size of the phase 2 stroke was therefore estimated as $(L2 - s_{fil}.\Delta T)$ and the filament sliding velocity in phase 2 as $(L2 - s_{fil}.\Delta T)/t2$.

Fiber compliance during steady shortening against different loads was measured in Florence by imposing 4 kHz length oscillations, $\sim$2 nm/half-sarcomere (hs) peak to peak, at the isometric tetanus plateau and after 40 nm/hs of steady shortening at 0.2−2 μm/hs/s. Elastic and viscous components of complex compliance were determined by Fourier analysis of force and sarcomere length sampled at 200 kHz. Viscous stiffness was less than 1% of elastic stiffness. Fiber cross-sectional area was 20,000 ± 3,000 μm^2 (SD, n = 4 fibers).

To induce the rigor state, intact fibers were transferred to Ringer's solution containing 20 mM butanedione monoxime (BDM), cooled to 1°C, and then 1 mM iodoacetic acid, 5.6 mM 2,4-dinitrofluorobenzene, and 1 mM sodium azide were added. After rigor induction was complete, as determined by stiffness measurements, fibers were returned to Ringer's solution with BDM, then to Ringer's solution. This protocol maintained sarcomere order, cell-membrane integrity, and strong tendon attachments.

X-Ray Data Collection

Fibers were mounted vertically in Ringer's solution at 4°C between mica windows carrying the stimulating electrodes, 600 μm apart on either side of the fiber, at the BioCAT beamline of the Advanced Photon Source (Irving et al., 2000b). Fiber cross-sectional area was 20,000 ± 7,000 μm^2 (SD, n = 15 fibers) and isometric force (T_0) was 240 kPa. X-ray exposure was controlled by two electromagnetic shutters in tandem, and monitored with 10 μs resolution using a pin diode. The wavelength was 0.1 nm and the maximum X-ray flux at the fiber was ca 2.10^{13} photons/s. The beam was attenuated for fiber alignment. Radiation damage was minimized by translating the fiber vertically between X-ray exposures by ca 100 μm. Data were typically collected from about 40 activations without effect on fiber function. X-ray diffraction patterns were collected on a cooled CCD detector (Phillips et al., 2002) mounted 2.5 m from the fiber. The 7000 vertical pixels were binned by two and the 4000 horizontal pixels by 32 before readout. The X-ray beam was focused at the detector with full width half maximum (FWHM) 50–80 μm vertically and 150 μm horizontally. The FWHM of the vertical point-spread function was 65 μm.

Experimental Protocols

X-ray data were collected at the end of phase 2 of the load-step response, at the end of phase 3, and at different times during phase 4. For phase 2 and phase 3, data from a series of load release/restretch cycles of period 50–100 ms were accumulated on the CCD (Reconditi et al., 2004). X-ray exposure time was 0.25–2 ms for phase 2 and 0.5–5 ms for phase 3, depending on the load. The restretch time was also adjusted according to the duration of phase 2 or 3 at the different loads. During phase 4, data were collected at times corresponding to shortening of about 20, 30, and 40 nm/hs, and X-ray exposure was 2.5 ms for load steps to 0.14 and 0.25 T_0, 5 ms for 0.5 and 0.75 T_0, and 10 ms for 0.88 T_0. X-ray data were also recorded from tetani with the same

protocols but without imposed length steps, and in 5 ms windows at 260 ms in separate isometric tetani. There were no significant differences between these two isometric patterns.

X-Ray Data Analysis

Diffraction patterns were dark-corrected, and then centered and aligned using the M3 and equatorial 1,1 reflections. The distribution of diffracted intensity along the vertical axis of the X-ray pattern, parallel to the muscle fiber axis, was calculated by integrating the 2D data from 0.017/nm on either side of the axis. Background intensity was subtracted after straight-line or smooth convex hull fitting. The interference components of each reflection were extracted by fitting multiple Gaussian peaks to the vertical intensity distribution. The total reflection intensity was calculated as the sum of the component peaks, and the spacing as the weighted mean of the component peaks, calibrated by that of the M3 reflection in an isometric tetanus, 14.573 nm (Linari et al., 2000). X-ray data analysis used the software packages Fit2D (A. Hammersley, European Synchrotron Radiation Facility) and Peakfit (SPSS Science).

Supplemental Data

Supplemental Data include one figure and can be found with this article online at http://www.cell.com/cgi/content/full/131/4/784/DC1/.

REFERENCES

Barclay, C.J. (1998). Estimation of cross-bridge stiffness from maximum thermodynamic efficiency. J. Muscle Res. Cell Motil. 19, 855–864.

Capitano, M., Canepari, M., Cacciafesta, P., Lombardi, V., Cicchi, R., Maffei, M., Pavone, F.S., and Bottinelli, R. (2006). Two independent mechanical events in the interaction cycle of skeletal muscle myosin with actin. Proc. Natl. Acad. Sci. USA 103, 87–92.

Cooke, R. (1997). Actomyosin interaction in striated muscle. Physiol. Rev. 77, 671–697.

Cooke, R., and Franks, K. (1980). All myosin heads form bonds with actin in rigor rabbit skeletal muscle. Biochemistry 19, 2265–2269.

Craig, R. (1977). Structure of A-segments from frog and rabbit skeletal muscle. J. Mol. Biol. 109, 69–81.

Dawson, M.J., Gadian, D.G., and Wilkie, D.R. (1978). Muscular fatigue investigated by phosphorus nuclear magnetic resonance. Nature 274, 861–866.

Decostre, V., Bianco, P., Lombardi, V., and Piazzesi, G. (2005). Effect of temperature on the working stroke of muscle myosin. Proc. Natl. Acad. Sci. USA 102, 13927–13932.

Dobbie, I., Linari, M., Piazzesi, G., Reconditi, M., Koubassova, N., Ferenczi, M.A., Lombardi, V., and Irving, M. (1998). Elastic bending and active tilting of myosin heads during muscle contraction. Nature 396, 383–387.

Dominguez, R., Freyzon, Y., Trybus, K.M., and Cohen, C. (1998). Crystal structure of a vertebrate smooth muscle myosin motor domain and its complex with the essential light chain: visualization of the pre-power stroke state. Cell 94, 559–571.

Ford, L.E., Huxley, A.F., and Simmons, R.M. (1977). Tension responses to sudden length change in stimulated frog muscle fibres near slack length. J. Physiol. 269, 441–515.

Geeves, M.A., and Holmes, K.C. (2005). The molecular mechanism of muscle contraction. Adv. Protein Chem. 71, 161–193.

Hanson, J., and Huxley, H.E. (1953). Structural basis of the cross-striations in muscle. Nature 172, 530–532.

Holmes, K.C. (1997). The swinging lever-arm hypothesis of muscle contraction. Curr. Biol. 7, R112–R118.

Holmes, K.C., Angert, I., Kull, F.J., Jahn, W., and Schroder, R.R. (2003). Electron cryomicroscopy shows how strong binding of myosin to actin releases nucleotide. Nature 425, 423–427.

Huxley, A.F. (1957). Muscle structure and theories of contraction. Prog. Biophys. Biophys. Chem. 7, 255–318.

Huxley, H.E. (1969). The mechanism of muscle contraction. Science 164, 1356–1366.

Huxley, H.E., and Brown, W. (1967). The low-angle X-ray diagram of vertebrate striated muscle and its behaviour during contraction and rigor. J. Mol. Biol. 30, 383–434.

Huxley, A.F., and Simmons, R.M. (1971). Proposed mechanism of force generation in striated muscle. Nature 233, 533–538.

Huxley, A.F., and Tideswell, S. (1996). Filament compliance and tension transients in muscle. J. Muscle Res. Cell Motil. 17, 507–511.

Huxley, A.F., Lombardi, V., and Peachey, L.D. (1981). A system for fast recording of longitudinal displacement of a striated muscle fibre. J. Physiol. 317, 12P–13P.

Huxley, H.E., Simmons, R.M., Faruqi, A.R., Kress, M., Bordas, J., and Koch, M.H.J. (1983). Changes in the X-ray reflections from contracting muscle during rapid mechanical transients and their structural implications. J. Mol. Biol. 169, 469–506.

Huxley, H.E., Stewart, A., Sosa, H., and Irving, T. (1994). X-ray diffraction measurements of the extensibility of actin and myosin filaments in contracting muscle. Biophys. J. 67, 2411–2421.

Huxley, H.E., Reconditi, M., Stewart, A., and Irving, T.C. (2006a). X-ray interference studies of crossbridge action in muscle contraction: evidence from quick releases. J. Mol. Biol. 363, 743–761.

Huxley, H.E., Reconditi, M., Stewart, A., and Irving, T.C. (2006b). X-ray interference studies of crossbridge action in muscle contraction: evidence from muscles during steady shortening. J. Mol. Biol. 363, 762–772.

Irving, M., Piazzesi, G., Lucii, L., Sun, Y.-B., Harford, J.J., Dobbie, I.M., Ferenczi, M.A., Reconditi, M., and Lombardi, V. (2000a). Conformation of the myosin motor during force generation in skeletal muscle. Nat. Struct. Biol. 7, 482–485.

Irving, T.C., Fischetti, R., Rosenbaum, G., and Bunker, G.B. (2000b). Fibre diffraction using the BioCAT undulator beamline at the Advanced Photon Source. Nucl. Instrum. Methods Phys. Res. A 448, 250–254.

Lan, G., and Sun, S.X. (2005). Dynamics of myosin-driven skeletal muscle contraction: 1. Steady-state force generation. Biophys. J. 88, 4107–4117.

Linari, M., and Woledge, R.C. (1995). Comparison of energy output during ramp and staircase shortening in frog muscle fibres. J. Physiol. 487, 699–710.

Linari, M., Dobbie, I., Reconditi, M., Koubassova, N., Irving, M., Piazzesi, G., and Lombardi, V. (1998). The stiffness of skeletal muscle in isometric contraction and rigor: the fraction of myosin heads bound to actin. Biophys. J. 74, 2459–2473.

Linari, M., Piazzesi, G., Dobbie, I., Koubassova, N., Reconditi, M., Narayanan, T., Diat, O., Irving, M., and Lombardi, V. (2000). Interference fine structure and sarcomere length dependence of the axial X-ray pattern from active single muscle fibers. Proc. Natl. Acad. Sci. USA 97, 7226–7231.

Lombardi, V., and Piazzesi, G. (1990). The contractile response during steady lengthening of stimulated frog muscle fibres. J. Physiol. 431, 141–171.

Lombardi, V., Piazzesi, G., and Linari, M. (1992). Rapid regeneration of the actin-myosin power stroke in contracting muscle. Nature 355, 638–641.

Lymn, R.W., and Taylor, E.W. (1971). Mechanism of adenosine triphosphate hydrolysis by actomyosin. Biochemistry 10, 4617–4624.

Molloy, J.E., Burns, J.E., Kendrick-Jones, J., Tregear, R.T., and White, D.C. (1995). Movement and force produced by a single myosin head. Nature 378, 209–212.

Nyitrai, M., and Geeves, M. (2004). ADP and strain sensitivity in myosin motors. Philos. Trans. R. Soc. Lond. B Biol. Sci. 359, 1867–1877.

Phillips, W.C., Stewart, A., Stanton, M., Naday, I., and Ingersoll, C. (2002). High-sensitivity CCD-based X-ray detector. J. Synchrotron Radiat. 9, 36–43.

Piazzesi, G., and Lombardi, V. (1995). A cross-bridge model that is able to explain mechanical and energetic properties of shortening muscle. Biophys. J. 68, 1966–1979.

Piazzesi, G., Reconditi, M., Dobbie, I., Linari, M., Boesecke, P., Diat, O., Irving, M., and Lombardi, V. (1999). Changes in conformation of myosin heads during the development of isometric contraction and rapid shortening in single frog muscle fibres. J. Physiol. 514, 305–312.

Piazzesi, G., Lucii, L., and Lombardi, V. (2002a). The size and the speed of the working stroke of muscle myosin and its dependence on the force. J. Physiol. 545, 145–151.

Piazzesi, G., Reconditi, M., Linari, M., Lucii, L., Sun, Y.-B., Narayanan, T., Boesecke, P., Lombardi, V., and Irving, M. (2002b). Mechanism of force generation by myosin heads in skeletal muscle. Nature 415, 659–662.

Rayment, I., Rypniewski, W., Schmidt-Base, K., Smith, R., Tomchick, D.R., Benning, M.M., Winkelmann, D.A., Wesenberg, G., and Holden, H.M. (1993a). Three-dimensional structure of myosin subfragment-1: a molecular motor. Science 261, 50–58.

Rayment, I., Holden, H.M., Whittaker, M., Yohn, C.B., Lorenz, M., Holmes, K.C., and Milligan, R.A. (1993b). Structure of the actin-myosin complex and its implications for muscle contraction. Science 261, 58–65.

Reconditi, M. (2006). Recent improvements in small angle X-ray diffraction for the study of muscle physiology. Rep. Prog. Phys. 69, 2709–2759.

Reconditi, M., Linari, M., Lucii, L., Stewart, A., Sun, Y.-B., Boesecke, P., Narayanan, T., Fischetti, R.F., Irving, T., Piazzesi, G., et al. (2004). The myosin motor in muscle generates a smaller and slower working stroke at higher load. Nature 428, 578–581.

Ruff, C., Furch, M., Brenner, B., Manstein, D.J., and Meyhofer, E. (2001). Single-molecule tracking of myosins with genetically engineered amplifier domains. Nat. Struct. Biol. 8, 226–229.

Sleep, J.A., Lewalle, A., and Smith, D. (2006). Reconciling the working strokes of a single head of skeletal muscle myosin estimated from laser-trap experiments and crystal structures. Proc. Natl. Acad. Sci. USA 103, 1278–1282.

Smith, D.A., Steffen, W., Simmons, R.M., and Sleep, J.A. (2001). Hidden-Markov methods for the analysis of single-molecule actomyosin displacement data: the variance-Hidden-Markov method. Biophys. J. 81, 2795–2816.

Steffen, W., Smith, D.A., Simmons, R.M., and Sleep, J.A. (2001). Mapping the actin filament with myosin. Proc. Natl. Acad. Sci. USA *98*, 14949–14954.

Takagi, Y., Homsher, E.E., Goldman, Y.E., and Shuman, H. (2006). Force generation in single conventional actomyosin complexes under high dynamic load. Biophys. J. *90*, 1295–1307.

Tyska, M.J., Dupuis, D.E., Guilford, W.H., Patlak, J.B., Waller, G.S., Trybus, K.M., Warshaw, D.M., and Lowey, S. (1999). Two heads of myosin are better than one for generating force and motion. Proc. Natl. Acad. Sci. USA *96*, 4402–4407.

Veigel, C., Bartoo, M.L., White, D.C., Sparrow, J.C., and Molloy, J.E. (1998). The stiffness of rabbit skeletal actomyosin cross-bridges determined with an optical tweezers transducer. Biophys. J. *75*, 1424–1438.

Veigel, C., Molloy, J.E., Schimtz, S., and Kendrick-Jones, J. (2003). Load-dependent kinetics of force production by smooth muscle myosin measured with optical tweezers. Nat. Cell Biol. *5*, 980–986.

Wakabayashi, K., Sugimoto, Y., Tanaka, H., Ueno, Y., Takezawa, Y., and Amemiya, Y. (1994). X-ray diffraction evidence for the extensibility of actin and myosin filaments during muscle contraction. Biophys. J. *67*, 2422–2435.